Review Article

Quantitative imaging of coronary blood flow

Adam M. Alessio[2], Erik Butterworth[3], James H. Caldwell[1,3] and James B. Bassingthwaighte[2,3]*

Departments of [1]Medicine, [2]Radiology and [3]Bioengineering, University of Washington, Seattle, WA, USA

Abstract

Positron emission tomography (PET) is a nuclear medicine imaging modality based on the administration of a positron-emitting radiotracer, the imaging of the distribution and kinetics of the tracer, and the interpretation of the physiological events and their meaning with respect to health and disease. PET imaging was introduced in the 1970s and numerous advances in radiotracers and detection systems have enabled this modality to address a wide variety of clinical tasks, such as the detection of cancer, staging of Alzheimer's disease, and assessment of coronary artery disease (CAD). This review provides a description of the logic and the logistics of the processes required for PET imaging and a discussion of its use in guiding the treatment of CAD. Finally, we outline prospects and limitations of nanoparticles as agents for PET imaging.

Keywords: *positron emission tomography (PET); coronary blood flow; myocardial perfusion; quantitative imaging; tissue clearance; blood-tissue exchange model; oxygen-15; ammonia N-13; gamma camera; SPECT*

1. Introduction to positron emission tomography (PET) and single photon emission computed tomography (SPECT) imaging

Modern non-invasive diagnostic imaging procedures have improved patient care by making earlier diagnoses with greater precision. X-radiography, using an external source of a beam of X-rays, paved the way, providing planar images of X-ray attenuation, or tissue density. These provided increasingly high spatial resolution as X-ray sources were made smaller and as film grain size was reduced. The next step transformed the field by using intravenous injections of gamma-emitting tracers to track and image cellular and organ functions. This modality depends on collimation to

Adam M. Alessio received his PhD in Electrical Engineering from the University of Notre Dame in 2003. During his graduate studies he developed tomographic reconstruction methods for correlated data and helped construct a high-resolution PET system. He is currently a Research Assistant Professor in Radiology at the University of Washington. His research interests focus on improved data processing and reconstruction algorithms for PET/CT systems with an emphasis on quantitative imaging.

Erik Butterworth recieved the BA degree in Mathematics from the University of Chicago in 1977. Between 1977 and 1987 he worked as a computer programmer/analyst for several small commercial software firms. Since 1988, he has worked as a software engineer on various research projects at the University of Washington. Between 1988 and 1993 he developed a real-time data aquisition for the analysis of estuarine sediment transport in the department of Geophysics. Between 1988 and 2002 he developed I4, a system for the display and analysis of cardic PET images in the department of Cardiology. Since 1993 he has worked on physiological simulation systems (XSIM from 1993 to 1999, JSim since 1999) at the National Simulation Resource Facility in Cirulatory Mass Transport and Exchange, in the Department of Bioengineering. His research interests include simulation systems and medical imaging.

define the direction of allowable photons that reach the crystal detectors. While gamma camera images were initially only planar, like the X-ray of the time, gamma photons are emitted from radioactive decay in random directions in 3-space. Subsequent rotating gamma cameras have provided 3D images based upon tomographic reconstructions from multiple views: this is single photon emission-computed tomography (SPECT).

Positron-emitting tracers allow a next step, even though they are short-lived and cannot be detected directly outside the body. When positrons are emitted, they travel about a millimeter and are then annihilated, giving rise to the emission of two gamma photons, which readily penetrate tissue and are detected outside by arrays of crystals. Positron emission tomography (PET) should probably have been called dual photon ECT (DPECT), but PET is expressive and efficient. The key is that the two photons are emitted in opposite directions, therefore when detected simultaneously in a pair of crystals, one knows that they came from somewhere on the line between the two crystals. This greatly improves the spatial resolution. Because gamma-emitting and positron-emitting tracers can be incorporated into a wide variety of molecules of biological interest, the developments opened a field of biochemical exploration – molecular medicine.

In this review, we offer a brief introduction to the physics and applications of these two imaging modalities, with a focus on quantitative cardiac PET imaging. Interested readers are directed to other sources for in-depth discussions of the physics, chemistry, and applications of PET and PET/CT (1–5).

1.1. Basic physics of positron emission tomography (PET) imaging

PET imaging requires producing a positron-emitting radioisotope. These may be made in a cyclotron by bombarding stable nuclei with high-energy particles. The

James H. Caldwell, MD, University of Missouri-Columbia 1970, is Professor of Medicine (Cardiology) and Radiology and Adjunct Professor of Bioengineering at the University of Washington School of Medicine and Acting Head, Division of Cardiology and Director of Nuclear Cardiology for the University of Washington Hospitals, Seattle WA, USA.

James B. Bassingthwaighte, MD, Toronto 1955, PhD Mayo Grad Sch Med 1964, was Professor of Physiology and of Medicine at Mayo Clinic until 1975 when he moved to the University of Washington to chair Bioengineering. He is Professor of Bioengineering and Radiology. In 1979, he established a National Simulation Resource Facility in Circulatory Mass Transport and Exchange and in 1997, he initiated the Human Physiome Projects. He is a member of the US National Academy of Engineering. His research is on quantitative integration of cellular and cardiovascular systems.

isotopes are then synthesized with biologically meaningful materials to form a radiotracer, or radiopharmaceutical. This process essentially 'labels' a substance that has a desired physiologic behavior. Numerous radiotracers have been developed for a wide range of applications. Table 1 presents some of the common radiopharmaceuticals.

As a positron-emitting radioisotope decays to a stable state it emits the positron (positive beta particle) that travels only a short distance before being annihilated on contact with an electron (negative beta particle) as in

Table 1. Common radiopharmaceuticals for PET

Application	PET probe	Mechanism
Glucose metabolism	[F-18] fluorodeoxyglucose (FDG)[a]	Accumulates as sugar phosphate
Bone scanning	[F-18] fluoride*	Incorporation into bone
Blood flow	[N-13] ammonia*	Accumulates as glutamate
	[Rb-82] rubidium*	Cell accumulation like potassium
	[0-15] H_2O	Inert highly diffusible indicator
	[F-18] BMS-747158-02	Inhibitor of mitochondrial complex I
	[Cu-62] PTSM	Diffusible indicator with multiple retention mechanisms (mitochondrial reduction, enzymatic, etc.)
Hypoxia	[F-18] fluoromisonidazole (FMISO)	Redox indicator shows hypoxia
Proliferation	[F-18] fluorothymidine (FLT)	Incorporation into DNA
Fatty acid oxidation	[C-11] acetate	Uptake and clearance by FA oxidation
Protein metabolism	[C-11] choline	Incorporation into phospholipids

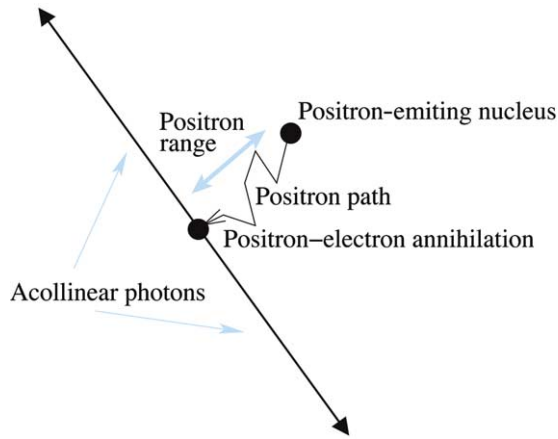[a]PET radiopharmaceuticals with FDA approval for certain clinical applications (17, 18).

Fig. 1. Basic principle of PET imaging: decay of radio-nuclide, positron emission, multiple scatters, annihilation with electron, and production of two collinear 511-keV photons. (Not to scale.)

Fig. 1. The distance, generally less that 2 mm, depends on the particular emission energy of the isotope and on the density of the tissue. The annihilation produces two 511 keV photons that travel at light speed in opposite directions very close to 180 degrees from each other. The PET scanner detects these photons by their near simultaneous detection with the crystal array, providing the location of the annihilation. Thus, PET scanners do not image the origin of the positron decay, but rather the location of the positron-electron annihilation.

Fig. 2 illustrates the overall process. The positron-labeled tracers are usually injected intravenously into the patient and distribute throughout the body, exchanging between blood and tissue, and then binding or participating in metabolic reactions, that is, becoming localized in accord with the physiological circumstances, and decay exponentially with time. The 511-keV photons leave the annihilation site, travel through the body, and, in the

ideal case, are detected by the scanner. The scanner contains a ring of scintillation detectors, which surround the patient. When one photon enters a detector, it produces a small amount of light, which is amplified into an electrical signal and is detected as a single count. After receiving one single count, the system waits some nanoseconds for another single count to occur in another detector. If two single counts occur in this prescribed time interval, these photons are paired together and the system stores it as a coincident event. This coincident event signifies that an annihilation occurred somewhere along the line connecting the two single detections. The line connecting two detectors is referred to as a line-of-response. (When time-of-flight detection is used, the difference in arrival times defines the position of the annihilation event within about 10 cm.) After the collection of numerous photons, a single line-of-response effectively measures the integral of annihilations along a single line through the patient. These lines in a single transaxial plane are organized by their azimuthal angle and radial distance (as illustrated in Fig. 2) and stored in a 2D matrix called a sinogram (a single annihilation site will map a sine wave in the sinogram domain). The sinogram is the Radon transform of the annihilation distribution in the object and is conceptually the same data space used in all tomographic modalities (6).

Tomographic reconstruction methods are employed to reconstruct images from sinogram data. In general, images are formed for each slice and then stacked together to form 3D image volumes. There are numerous methods for tomographic reconstruction and all seek to perform some variant of the inverse Radon transform of the raw sinogram data. The leading approaches for clinical PET include filtered back-projection (FBP) (6) and ordered subsets expectation maximization (OSEM) (7) The FBP method is analytic, offering a fairly simple formula for the inverse Radon transform. This method offers a fast solution at the expense of less desirable noise
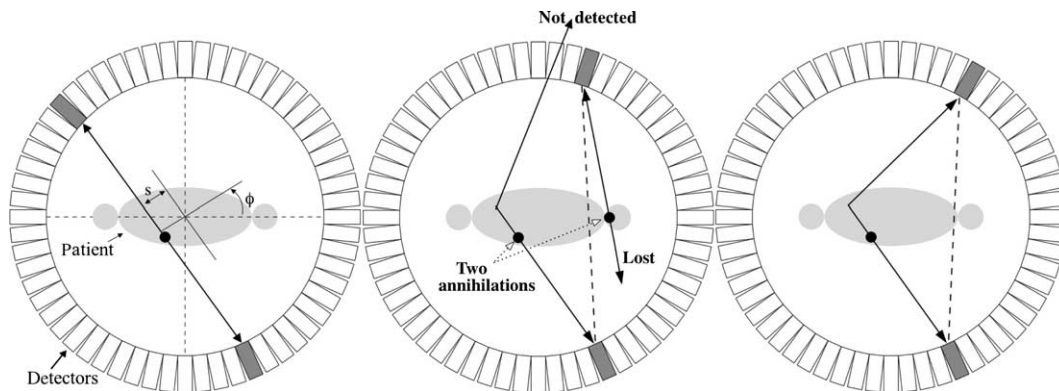

Fig. 2. Transaxial view of ring of detectors and patient demonstrating the types of coincident events. (A) True coincidence. (B) Random (accidental) coincidence. (C) Scattered coincidence. The annihilations marked with solid black dots do not occur along the detected line-of-response in the second two cases leading to increased systemic noise in the data.

properties and is currently the workhorse of image reconstruction in X-ray computed tomography (CT). The OSEM method is an iterative method that seeks to find the maximum likelihood solution for the image based on a Poisson statistical model of the data. The OSEM method is more computationally intensive, but offers potentially better signal to noise properties.

1.2. Factors degrading image quality in positron emission tomography (PET)

As with all modalities, PET has physical limitations that limit its signal to noise performance. The previous description focused on the ideal case. In reality, as the 511-keV photons travel through tissue, many of them interact through Compton scattering (and with small probability through photoelectric effect) and change their direction. These interactions cause deviation from a straight path, resulting in 'attenuated' photons. The probability that a photon will travel along a straight line is given by

$$P(x') = \exp\left(-\int_0^{x'} \mu(x)dx\right),$$

here x is the location along the line from 0 to x' through the patient with different linear attenuation coefficients, $\mu(x)$. The attenuation coefficients vary based on the type of tissues in the imaged volume and the energy of the incident photons. X-ray imaging measures variation in attenuation. PET imaging attempts to measure the location of the radiotracer and attenuation confounds this information. In whole-body PET imaging, as much as 90% of the coincident events are lost due to attenuation. PET systems have dedicated components to obtain an attenuation map of the imaged volume in each individual patient. Standalone PET scanners have a transmission, rotating, radioactive rod source that essentially performs a low-resolution CT scan using the PET detectors. PET/CT scanners use the CT component to form the attenuation map (8). The attenuation map of the patient is forward projected into the same data space as the PET data and applied as an attenuation correction.

If one or both of the annihilation photons scatter before detection, then the scanner could incorrectly position the event. Fig. 2C illustrates the mispositioning error of these scattered coincident events. Scattered events can account for as much as 40% of the detected events in a whole-body acquisition and result in an increased background noise in the PET image. Reduction and correction algorithms for scattered events can reduce the bias caused by position-dependent scatter, but cannot fully remove this major contributor to background noise (9, 10).

Another source of noise in PET are random events caused by the incorrect pairing of photons from different annihilations. As shown in Fig. 2B, random events arise from a variety of situations, such as the highly likely attenuation of one photon or when the system fails to detect a photon. As with scatter correction, randoms correction algorithms can alleviate some but not all of the noise contribution of this physical limitation (11).

The noise in PET depends on the number of events detected. This count-limited modality benefits from the long acquisition times needed to acquire as many true events as possible. Increased injected activity will not only result in a beneficial linear increase in true events, but also in a detrimental linear increase in scatter events and a highly detrimental square increase in random events. PET systems and acquisition protocols are designed to optimize the tradeoffs of true, scatter, and random events (12). But it is obvious that rapid transients in local tissue concentrations will involve a tradeoff between the accuracy of each image acquired and the number of events recorded. Later, we discuss this tradeoff, noting that transients are best handled using very short time-windows in order to avoid distortion of the true time course, even though the time-activity curves (TAC) appear relatively noisy.

In terms of signal strength, the resolution of PET will always be limited by the nature of positron annihilation (13). As positrons travel through tissue, they experience multiple interactions (mostly Coulomb) until their kinetic energy reduces to thermal energies and they annihilate with an electron. Higher energy positrons travel farther from the site of decay than lower energy positrons. One way to characterize this positron range for an isotope is the radius that includes 75% of all annihilation events. For common PET isotopes, this radius is between 1.2 mm for F-18 and 12.4 mm for Rb-82. Furthermore, the photons leaving the site of annihilation are slightly non-collinear (within 0.23°) (14). In current whole-body PET tomographs with a ring diameter of 70 cm, non-collinearity results in an effective resolution loss of approximately 1.5 mm.

Along with these inherent physical limitations, the detection system introduces resolution limitations (15). The detectors contain scintillation crystals that stop the 511-keV photon and convert its energy into detectable light. The emitted light then travels through the crystal and into photomultiplier (PMT) tubes for amplification and coincidence detection, thereby defining the line between the detectors giving positioning. Detectors have an intrinsic spatial resolution that depends upon several factors, including density of crystal, thickness, light guide type, and PMT performance. When individual detectors are combined in a full system, inter-crystal penetration, when a photon enters one crystal and continues to a neighboring crystal, is a common problem. In conventional whole-body systems with a cylindrical ring of detectors, photons traveling along paths at the edge of the transaxial field of view can be incorrectly assigned

due to penetration into neighboring crystals. This edge of the field of view mispositioning is commonly called parallax error.

1.3. Positron emission tomography/computed tomography (PET/CT)

The first PET/CT scanner was introduced in 1998, providing a single device with both 'functional' (PET) and 'anatomic' (X-ray CT) imaging capabilities (16). These systems consist of essentially separate PET and CT subsystems and a shared patient bed to provide a shared coordinate system. This design allows for simple 'hardware' alignment of the PET image of radiotracer distribution and the CT image of tissue attenuation, providing high-resolution anatomic detail. Together with the primary benefit of aligned functional and anatomic images, the CT scanner also provides a fast, relatively noise-free attenuation map for PET attenuation correction. These combined systems have developed into the industry standard for PET imaging, and the majority of current commercial, clinical PET systems are now PET/CT systems.

1.4. Common applications of positron emission tomography (PET)

The majority of PET scans are performed for cancer imaging with ^{18}F-fluorodeoxyglucose (FDG). FDG is transported into cells, phosphorylated via a hexokinase, like glucose, and is trapped in the cells as FDG 6-phosphate. Hydrolysis via glucose-6-phosphatase is substantial in the liver and kidney, but the heart and brain have little of the enzyme. In the macroscopic view, FDG is distributed in the body based on local rates of glucose consumption. Considering that many tumors are hypermetabolic and preferentially use glucose, increased FDG can highlight the presence of rapidly growing tumor cells. Fig. 3 presents an example of a whole-body FDG image showing the normal distribution of FDG in tissues throughout the body, including increased uptake in the bladder. The abnormal focal uptake in the abdomen highlights hypermetabolic cancerous cells in the left lobe of the liver and upper abdominal lymph nodes.

PET can also be used to image several tracers for myocardial perfusion. For example, ^{13}N-ammonia (NH$_3$) is metabolically trapped in tissues and preferentially accumulates in regions with increased blood flow. This mechanism will be discussed in detail later. Fig. 4 presents an example from a cardiac ammonia examination. Note that the isotope distribution is different from the FDG distribution, as the mechanism and meaning of the trapping is quite different. Table 1 presents a small sample of PET radiopharmaceuticals.
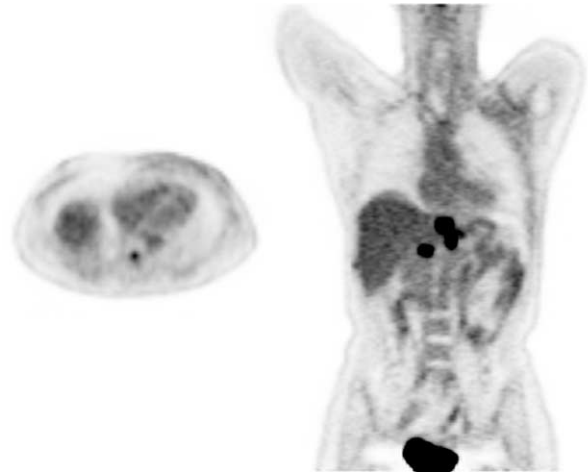

Fig. 3. Example images from a whole-body FDG PET examination. Transaxial image of the heart slice on the left is one of many slices stacked together to form an image volume, which is multiplanar reformatted into the single coronal view (neck to thighs) on the right.

1.5. Single photon emission computed tomography (SPECT) imaging

Single photon imaging began when Marie Curie obtained an image of a radium-containing rock on film, but had its real evolution in the 1950s with the manufacture of the Anger camera, containing large planar sodium iodide crystals backed by arrays of photodiode detectors. Patient images were obtained by positioning the camera over the patient. Insertion of a collimator between the emission source and the detector scintillation crystal improved the image so that it represented a projection of the radiation source concentrations in the tissue. Thus, the image represented the concentrations through the depth of the tissue along the lines of the collimation, but with some degradation due to scatter within the tissue, absorption within the collimator itself, and the finite spatial resolution of the scintillator crystal and the PMT array.
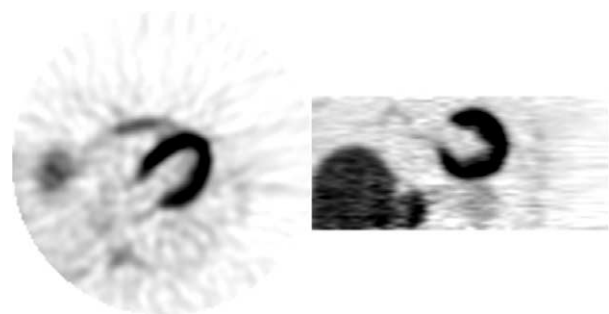

Fig. 4. Example images from a cardiac N-13 ammonia PET examination. The left image is a transaxial image of the heart slice showing increased ammonia uptake in the myocardium. The right image is the coronal view (shoulder to base of liver) showing uptake in the myocardium and liver.

The highest spatial resolution with a parallel-collimator gamma camera is obtained by putting each slice of tissue directly on the collimator face, then reconstructing the 3D object from the multiple slices. We used this technique to assess regional myocardial flow distributions of macroaggregated albumin during regional ischemia (19). Later, 15 μ microspheres improved the resolution in such studies (20a). Only much later was the microsphere method demonstrated to have almost as good resolution for defining regional flows as the use of completely deposited molecular markers (20b).

The gamma (Anger) camera evolved into a SPECT system by rotating the camera around the patient, stopping every few degrees to get a projection, and then reconstructing using FBP. The acquisition speed was increased by using two and then three camera heads (collimated detector and PMT array). The SPECT collimator stops photons traveling along oblique lines, allowing for the detection of photons along known lines of response. In PET, there is no need for hardware collimation since lines of response are formed from the pairing of two co-linear photons. Thus, PET is generally more sensitive than SPECT, has less noise, and higher resolution.

In addition to static planar imaging and SPECT imaging, the same equipment can be used for planar dynamic imaging, where a sequence of images is acquired over time. A common application is to measure renal clearance, i.e. glomerular filtration rate. Sequential, timed images demonstrate where the indicator is in the renal cortex, then in the medulla and renal pelvis, and finally in the bladder. Another common use of single photon protocols is gated imaging of the heart, using ECG signals to time several distinct periods over which the data are acquired during the cycle of systolic contraction and diastolic relaxation. These multiple-gated acquisition (MUGA) scans provide an accurate, non-invasive means to measure left ventricular (LV) ejection fraction. New dedicated cardiac SPECT cameras are being developed to form a volumetric image without the need to rotate the camera heads, and will be useful in imaging cardiac tracer kinetics.

2. Positron emission tomography (PET) and coronary artery disease (CVD)

Numerous diagnostic modalities are available to assess the presence, severity, location, and origin of coronary artery disease (CAD), with coronary angiography (with X-ray) currently established as the leading method to define the arterial anatomic state. PET imaging has been employed to evaluate numerous cardiac pathologies, including myocardial glucose uptake and viability with ^{18}F-FDG, muscarinic receptor location with ^{11}C-MQNB, sympathetic function with ^{11}C-meta-hydroxyephedrine, and β-adrenergic receptor density with ^{11}C-CGP 12177.

We focus this discussion on the most common application of PET in cardiac imaging: assessment of myocardial blood flow (MBF) using ^{13}N-NH$_3$, ^{82}Rb, or ^{15}O-water.

In clinical practice, regional MBFs assessed with SPECT and PET identify regions of reduced flow as 'cold spots,' where there is low deposition of tracer. Usually two doses are given a half-hour or more apart to estimate regional perfusion under rest and stressed conditions. Stress testing involves injecting a vasodilator stress agent, such as dipyridamole or adenosine, to assess whether or not coronary stenoses prevent the normal increases in coronary flow. A comparison of stress and rest flows provides valuable information regarding the ability of the coronary arteries to reach maximal flow. In addition, the extent and severity of any abnormality provides important intermediate term (3 months to 3 years) prognostic information as to the probability of death or myocardial infarction (21–23).

The most common clinical nuclear stress tests are performed with SPECT scanners. SPECT imaging is the leading perfusion imaging method because of the availability of radiotracers and scanners that are less expensive than for PET. SPECT imaging provides a qualitative regional perfusion map in which disease is assessed based on the relative apparent uptake among different regions of the heart. SPECT has a high sensitivity, 90–94% for multivessel coronary disease. It is less sensitive, 60–76%, for single-vessel disease (24, 25). Given that SPECT depends on qualitative, relative differences in uptake, it is not good for assessing balanced ischemia in which diffuse disease is present in all three coronary vessels. This is part of the reason for its rather poor sensitivity (26).

A nuclear stress test with PET offers several advantages over SPECT. Numerous detailed clinical comparisons of cardiac SPECT and PET have been performed (27–29). In general, SPECT imaging is inferior to PET owing to poorer spatial resolution, because resolution is dependent on the distance from the detectors, and the inherent difficulty of performing attenuation correction in SPECT. PET has been shown to have improved specificity in obese patients (84% PET versus 69% SPECT) (30). In practice, PET examinations reduce diagnostic uncertainty compared to SPECT (29, 31). An additional major benefit of PET over SPECT is that it has a higher temporal resolution allowing for the acquisition of a dynamic series to image the kinetics of the radiotracer through the heart. This dynamic imaging capability permits the absolute quantification of blood flow as discussed later. Quantification of absolute flow is particularly important in patients with balanced disease in all coronary vessels or microvascular disease (e.g. diabetes, hypertension), where there are no regions that can serve as a 'normal' reference.

To provide a sense of the basic steps of a cardiac PET imaging protocol, Fig. 5 illustrates the components of a
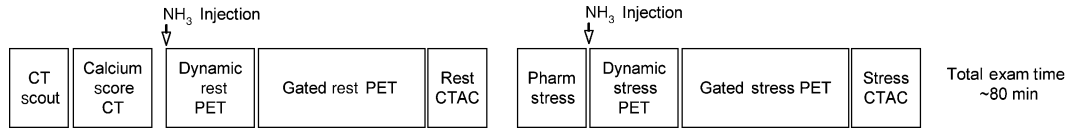
Fig. 5. Example cardiac N-13 ammonia PET/CT acquisition protocol for regional myocardial blood flow, rMBF. CTAC = cardiac time–activity curves.

typical ^{13}N-NH$_3$ PET/CT imaging examination. PET/CT imaging sessions begin with a CT scout scan to determine the scan range of subsequent acquisitions. Then, additional CT acquisitions can be performed, such as a calcium score CT, to provide additional diagnostic side-information. The ^{13}N-NH$_3$ is prepared by cyclotron bombardment and purification. After intravenous injection, a series of PET images are acquired over multiple time frames. From the image intensities in chosen regions of interest (ROI), we obtain time–activity curves (TAC) of tracer concentration over 2–3 min. The TAC are the 'raw' information used to estimate absolute MBF within that ROI. Then, a PET acquisition with cardiac gating is performed to generate qualitative maps of blood flow across a cardiac cycle along with assessment of global and regional ventricular function. Finally, a CT is performed for attenuation correction of the PET images. This procedure is used to obtain data on the patient at rest and again after pharmacologic stress to determine the responsiveness of the coronary arteries to an increased demand for oxygen delivery.

2.1. Why quantify myocardial blood flow (MBF)? Won't the qualitative image suffice for diagnosis?

Nuclear stress scans conventionally rely on qualitative measurements of regional perfusion determined through relative regional differences in uptake. Qualitative images have certainly proven useful in the detection of coronary artery disease, prognosis, and clinical management of patients. The quantification of the regional blood flow adds value to the qualitative information as summarized in Table 2.

Table 2. Applications of myocardial blood flow (MBF) quantification

1. Verify success of pharmacologic stress
2. Detection of global and regional disease
3. Evaluation of extent of multivessel disease
4. Evaluation of balanced coronary stenoses
5. Evaluation of microvascular disease
6. Evaluation of endothelial function
7. Monitor therapy
8. Tool to understand coronary physiology

Note: Adapted from Reference (32).

2.2. Background on quantitative myocardial blood flow (MBF) estimation with positron emission tomography (PET)

Estimation of MBF is done through modeling analysis of the regional TAC of tissue tracer content following injection upstream. The input function is obtained from the tracer concentration-time curve upstream to the coronary inflow, namely from the with left ventricular (LV) or left atrial (LA) TAC data. Numerous tracers have been used for rMBF estimation with PET: ^{15}O-water (diffusible) (33), ^{13}N-NH$_3$ (diffusible/metabolized/ retained) (34, 35), ^{11}C-acetate (extracted/metabolized) (36), and ^{82}Rb (extracted/retained) (37). Along with these accepted tracers, new ^{62}Cu and ^{18}F labeled agents are being explored for potentially less expensive, higher quality MBF estimates (38, 39). A thorough comparison of PET flow agents is presented by deKemp et al. (40).

The gold standard for flow measurements is ^{15}O-water because it is flow-limited in its exchange between plasma and tissue (52). Unfortunately, this agent must be produced in a cyclotron and has a short half-life (2.03 min), limiting its widespread use and the amount of activity that can be delivered to the patient. ^{13}N-NH$_3$ has a longer half-life (9.97 min) and is almost freely exchangeable between plasma and cell cytoplasm at even high levels of flow, allowing its use as a reference standard for flow measurements. Because ammonia is converted to ^{13}N-glutamine and ^{13}N-glutamate and is retained for a long time in the myocardium, high-quality images can be obtained from the accumulation of counts a few minutes after injection. ^{82}Rb has a short half-life (1.27 min), but this isotope offers the clinical convenience of production from a parent generator (strontium-82, with half-life 25 days). The generator is a less expensive source than a cyclotron and can be positioned close to the patient, facilitating higher dose injections. Although the extraction fraction for ^{82}Rb is only 70–80% and lower in high flow regions, it is still high enough for both image interpretation and for the approximate estimation of flow.

Capillary-tissue exchange models accounting for intracapillary concentration gradients and permeation of the capillary and cell membrane have been in use for years for both multiple indicator dilution studies and for PET studies (41–43). Somewhat different blood flow models have been used for the several PET tracers. In blood-tissue exchange processes as the solute leaves the blood to cross

the endothelial barrier and interstitial fluid regions to enter the parenchymal cells of an organ or tissue, the tracer concentrations diminish along the length of the capillary, diminishing the effluxes, which are simultaneously being reduced by back-diffusion from the interstitial fluid into the blood as in Fig. 6. Incomplete but simple 'one-compartmental models,' which assume that the blood content of the region of interest is negligible and that the tissue components all have the same concentration from capillary entrance to the exit, so-called 'lumped models,' have often been used for estimating flow. They use an input signal of a form either assumed or taken from and upstream TAC signal, e.g. left atrium, and have applied the one-compartment model to the analysis for ^{15}O-water (33), ^{13}N-NH$_3$ (44), ^{11}C-acetate (36), and ^{82}Rb (37). In these models, MBF is assumed proportional to the uptake rate constant K_1. The compartmental approximation was a simplification of the principles demonstrated by Crone (45) and Renkin (46), who showed that the capillary membrane permeability-surface area product, PS ml/(g min), for an axially extended capillary-tissue exchange region could be calculated simply when there was no return flux from tissue to the effluent blood:

$$PS = -F \log_e(1 - E_{\max}),$$

where F is flow (ml/(g min)) and $E_{\max}$ is the maximal extraction of tracer during the observation period. The extraction is conceptually similar to the extraction E given by arterio-venous difference divided by the inflow concentration in the steady state, and in the absence of return flux from tissue to blood, it is identical to it. But usually it is not the same, as the $E_{\max}$ for the tracer experiments of Crone and of Renkin and others represents a unidirec-

tional flux, whereas the steady state E represents the net flux. For example, the instantaneous extraction for ^{15}O-water is virtually 100%, but its steady state net flux is zero; likewise for the monovalent cations, Rb or K, the tracer maximum is 70–80% (and is very flow dependent), while, since neither is metabolized, the steady state net flux is zero. Experimentally, the maximum instantaneous extraction is defined relative to a simultaneously injected reference intravascular marker. When PS/F is very high, the extraction is close to 1, as the exponential term in the rearranged equation goes toward zero:

$$E_{\max} = 1 - e^{-PS/F}.$$

When PS/F (or in this case K_1/F) is greater than 4, then E is close to 1, as shown for water and for NH$_3$ in Fig. 7 (left panel), where the flux K_1 is the extraction times flow for each agent, plotted versus MBF. Fig. 7 (right panel) shows the curve of clearance of the tracer into the tissue for conditions when there is no return flux from tissue to blood, that is, when everything that crosses the capillary membrane into the tissue is retained. Each extraction curve plateaus at extraction times $F = PS$. These equations were derived for the analysis of experiments on the heart, brain, and skeletal muscle in which points were obtained at 1 sec time intervals and were relatively noise free. But because there is normally some reflux by passive diffusion back into the blood, further advances were required in the modeling to account for concentration gradients along the length of the capillary. Concentrations may diminish by factors of 10–100 along the capillary, which contradicts the idea of the uniform concentration assumed in using a compartmental stirred tank model.

Two compartment models have also been proposed for ^{13}N-NH$_3$ (34) and ^{82}Rb (47). These models include a simple retention model assuming that some of the tracer is retained without subsequent washout. Sensitivity analysis suggests that these models may result in highly variable parameter estimates unless certain values are constrained (37, 48). Likewise, a direct comparison of one and two compartment models for ^{13}N-NH$_3$ highlighted the understanding that there is a real difference between the two approaches (49).

The reason the one-compartment models can give reasonable estimates of flow in spite of their simplicity is that they provide an estimate of the mean transit time, t_{mean}. The PET and SPECT measures of regional flows are not absolute milliliters per second of coronary blood flow, but of 'perfusion flow' in milliliters per gram of tissue per second, which is more to the point, allowing us to understand metabolic rates of substrates and oxygen in terms of moles per gram of tissue per second. The flow per gram of tissue is F ml/(g.sec), when flow (ml/sec)
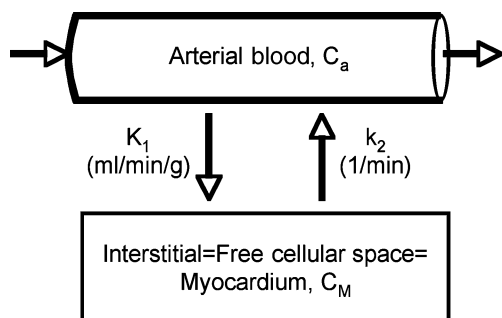

Fig. 6. Capillary-tissue exchange model simplified to two spatially distributed regions, the capillary blood and the extravascular tissue, composed of endothelial cells, the parenchymal cells of the tissue and the interstitial fluid space, here assumed to have similar concentrations throughout, as if the tracer were flow-limited in its exchange rates and not barrier- or membrane-permeation limited. One-compartment models ignore the blood content of the ROI and assume that upstream and downstream gradients are eliminated by rapid axial mixing in the tissue.

is normalized by the mass of the perfused region in grams, which is [r(g/ml) volume of tissue (ml)]. Thus, F ml/(g.sec)/V_{tiss} (ml/g) $= 1/t_{mean}$, showing that t_{mean} gives the desired meaningful physiological information. What is lost by using the compartmental models is the ability to fit the data functions precisely; also lost is the interpretability of other parameters, most notably the PS, the permeability surface area of the membranes and the volumes of distribution of the solutes. In more detailed models, these parameters can be estimated not only from high-resolution data such as from multiple indicator dilution curves, where one uses two or three tracers simultaneously, distinguishing the capillary space from the interstitial space and cell space, but also from PET data.

Along with the tracer kinetics, the blood flow models must include a correction for partial volume effects and blood pool spillover. The partial volume error is because the PET system has a limited spatial resolution, resulting in underestimation of uptake in small structures. In cardiac imaging, the variations in wall thickness (particularly in the setting of myocardial scar) and wall motion lead to bias in the regional estimates of the tracer. The blood pool spillover occurs because the time course data of the tracer is acquired and averaged over multiple cardiac cycles. The tracer in the left and right ventricular cavities, c_{blood}, often confounds the apparent tracer level in one portion of the myocardium. In the simplest models, these two degradations in the TAC are corrected with a single scalar, S, for spillover fraction, which can be estimated by optimizing the fitting of the model to the TAC for the ROI. Therefore, the TAC provided by the image sequence in the ROI, c_{region}, is the sum of the spillover fraction plus the activity of the region, $c_{myo}(t)$:

$$c_{region}(t) = S \times c_{blood}(t) + c_{myo}(t),$$

where S is the spillover correction factor (including partial volume) ranging from 0 to 1. In the modeling analysis, the solution of the equations represents $c_{myo}(t)$; the parameters to be adjusted are those of the model plus the magnitude of S.

2.3. Axially distributed models for quantification of myocardial blood flow

Because tracers of interest such as $^{13}NH_3$, ^{82}Rb, and ^{15}O-water must be transported across endothelial and myocardial cell membranes, and their retention is influenced by the cellular metabolic state (governing rates of retention and pool size), it is critical to account for the graded diminution in concentration along each capillary-tissue unit. This is done by using axially distributed models, accounting for uptake at each point along the capillary. (Stirred tank models collapse the gradients by assuming uniformity of concentration within a capillary 200 times as long as its diameter, thereby introducing systematic error into flow estimates.) The parameters of models are unchanged by the choice of using partial differential equations (PDEs) versus ordinary differential equations (ODEs), so the difference is in the numerical representation of the ideas. Accounting for the axial gradients using PDEs prevents the error implicit in the ODE representation that the tissue is a stirred tank and
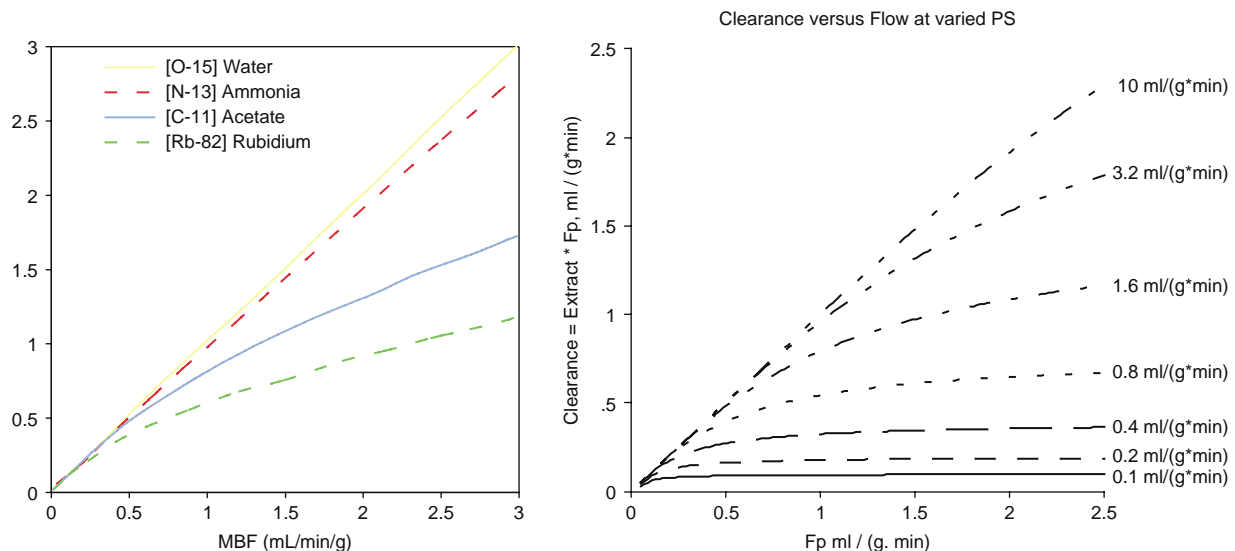

Fig. 7. (Left panel) Uptake parameter K_1 versus MBF used with a one-compartment model of tracer kinetics. Relationship between K_1 and MBF is flow-dependent and potentially dependent on disease status. Used with permission from Reference (40). (Right panel) clearance curves (extraction times flow) for tracers whose extracted fraction is totally trapped in the tissue. Plots are from an axially distributed blood-tissue exchange model. The curves plateau at Extract *Flow $=PS$, the permeability-surface area product for the solute.

that material just entering the capillary has the same chance of exiting into the outflowing vein as material that arrived earlier; by contrast, the PDE keeps the sequence of the inflowing concentrations, and doesn't slur the shape of the input.

An experimental study on an isolated blood-perfused rabbit heart from Deussen and Bassingthwaighte (50) illustrates the high temporal resolution that can be obtained with positron-emitting ^{15}O-oxygen. The setup is illustrated in Fig. 8: a bolus of blood labeled with ^{15}O-oxygen is injected into the inflow to the coronary system; the input and output TAC are recorded using scintillator detectors surrounding the inflow and outflow tubing; the residue function, the tracer content in the heart itself, is recorded by coincidence detectors on either side of the heart. The system is modeled using the PDEs for oxygen transport through the capillaries, its non-linear binding to oxygen, its transport across the membranes into the cells where it binds to myoglobin, and its metabolic transformation to ^{15}O-water; the ^{15}O-water exchange and washout is modeled with a similar set of PDEs, though not having to account for the binding. The results of using the observed input function and fitting the model simultaneously to the cardiac residue function data and to the observed output function are shown in Fig. 9. The axially distributed model gives quite precise fits to the data and gives good estimates of the oxygen consumption rate for comparison with measures obtained from arterio-venous differences and the measured blood flow.

In this situation, the transport of oxygen is mainly within the blood because of the high affinity binding to hemoglobin; therefore, oxygen has a short transit time through the heart, only a little more than that of indocyanine green (ICG), which is bound to albumin and remains strictly intravascular. The time between the peaks of the inflow and outflow curves for the ICG was about 14 sec (upper panel, Fig. 9), while the time between
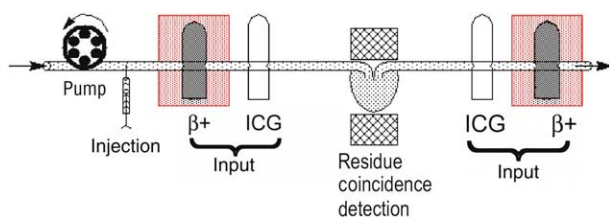

Fig. 8. Experimental setup for isolated blood-perfused rabbit hearts. ^{15}O-oxygen is injected into the inflow. Plastic scintillation detectors, β^+, and infrared indocyanine green detectors, ICG, measure input and output functions for the positron-emitting tracer and the plasma indicator. The heart is positioned in the center of the coincidence detection system (NaI (Tl-activated) crystals). (From Reference (50) with permission from the American Physiological Society.)

^{15}O-oxygen peaks was about 18 sec (middle panel, Fig. 9). In striking contrast, the peak of the outflowing ^{15}O-water curve was not reached at 60 sec (middle panel).

The blood flow was 0.8 ml/(g min). The expected mean transit time for ^{15}O-water is the tissue water space $(0.78 \pm 0.01$ ml/g) divided by the flow of intravascular water. The flow of water is the blood flow times water fraction of blood (Hct $\times w_{RBC} + (1 - $ Hct$) \times w_{pl}$), where Hct is hematocrit and w_x is the water fraction of red blood cells (RBC) or plasma (pl). For this experiment, the water fraction is 0.88, giving a flow of intravascular water of 0.70 ml/(g min) and a mean transit time of 0.78 (ml/g)/0.70 ml/(g min) or 1.1 min. Since the modeling uses these known fractions of blood and tissue as a part of the data set for the model fitting, the results are completely self-consistent.

2.4. Automation of quantitative regional flows for functional imaging

Several efforts have centered on automating the creation of functional images of regional flow distributions. These methods model blood flow to each of many ROIs in the myocardium. This process requires automating the positioning of the ROIs, the capturing of the TAC of the tracer within each defined region, the analysis by model fitting to the TAC to estimate the local flow, and the displaying of the acquired composite images and of the model estimates of the regional flows in the 3D heart. The bull's-eye polar map display invented by Caldwell (51) is color or intensity coded for the magnitude of the flow in each ROI and remains the most common method of display. The center of the bull's-eye is the apex of the LV and concentric rings around it represent the circumferential rings of tissue from apex toward the base of the heart. The mapping can also be done onto a 3D cardiac shape. These, with other patient-specific information, provide the basis for therapy decisions.

3. Future prospects: nanoparticles and positron emission tomography (PET)

While the majority of PET probes are formed with small molecules or macromolecules, there has been increasing interest in developing molecular imaging strategies using organic and inorganic nanoparticles (53). In comparison to other molecular imaging modalities, such as optical or targeted contrast-enhanced MRI, PET offers potentially superior sensitivity to smaller concentrations of molecular probes and the ability to quantify concentrations in absolute units. Nanoparticles have interior and exterior surfaces to which researchers have attached radionuclides for PET imaging (54) or specific ligands for targeting the delivery of the particles (55–57). It is this potential for delivering drugs to targeted locations or sites with
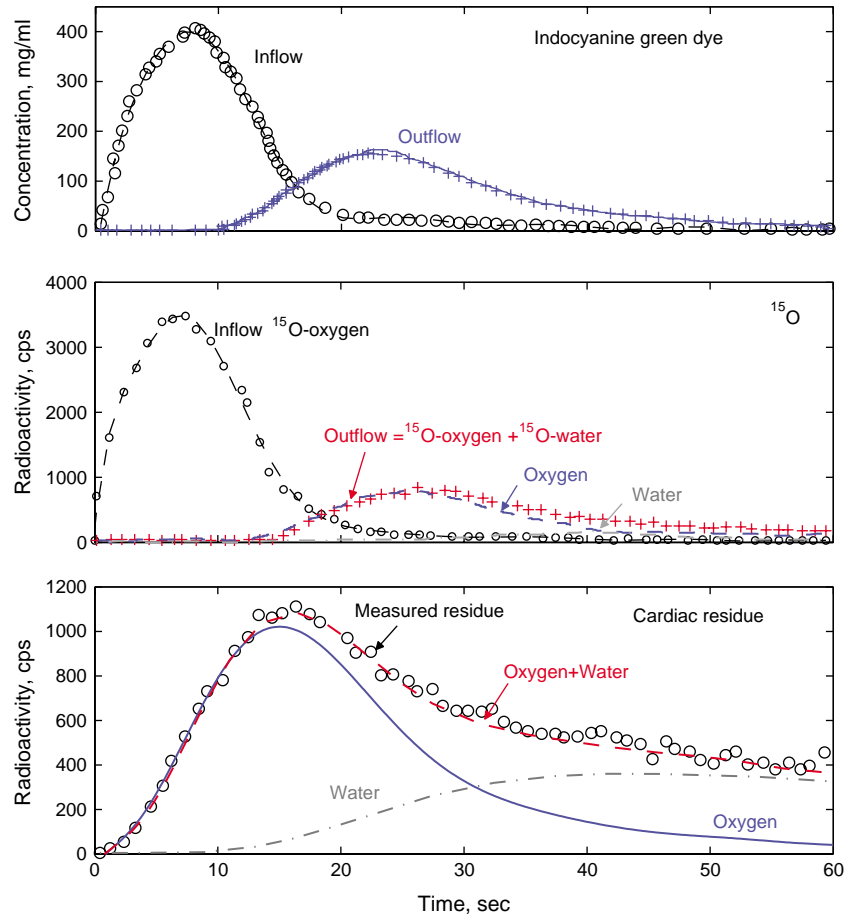
Fig. 9. Model fitting of ^{15}O-oxygen and ^{15}O-water time–activity curves after injection of bolus of ^{15}O-oxygen in blood of 20% hematocrit with blood flow = 0.8 ml/(g min). Top panel: ICG curves. Middle panel: ^{15}O-curves. Bottom panel: cardiac residue function (open circles) with model solutions for contents of ^{15}O-oxygen and ^{15}O-water. The oxygen consumption was 1.1 μmol g^{-1} min^{-1}. (From Reference (50) with permission from the American Physiological Society.)

ligand-specific affinities, combined with PET imaging, that can lead to combining the treatment and the monitoring of the localization of the agent. (For a thorough review of PET nanoparticles, readers are referred to the review by Welch et al. (58).)

An example of PET imaging of cardiovascular disease is a macrophage-tracking nanoparticle (59). This particle is formed from the monocrystalline iron oxide nanoparticle (MION) to which a near-infrared fluorochrome and positron-emitting Cu-64 are attached, allowing trimodality reporting with MRI, fluorescence, and PET. The dextran-coated nanoparticles undergo non-specific phagocytosis and accumulation in macrophages. Since macrophages are a common prominent constituent of atherosclerotic lesions (60), we speculate that nanoparticles might be useful in imaging or even in treating atherosclerotic lesions.

While there is much promise for nanoparticles in imaging and in the targeting of chemotherapeutic agents, toxicity may be a problem. Adding to the normal

concerns with drugs and contrast agents, one needs to be aware that nanoparticles larger than 5 nm can collect in the liver and spleen to reach toxic levels (61). Such concerns have motivated efforts to replace chemically stable particles with biodegradable ones.

4. Summary

PET provides volumetric images of radiotracer distribution. This modality is primarily employed for the detection of cancer and has proven valuable for numerous other clinical applications including the assessment of CAD. For CAD, both PET and SPECT can generate *qualitative* maps of MBF, but PET can generate *quantitative* maps of regional myocardial flows giving direct evidence on the effect of local coronary disease of atherosclerosis. Direct information on the atheromata is a further possibility. The high sensitivity and quantitative capabilities of PET imaging make it a promising modality for molecular imaging with nanoparticle-based probes.

Acknowledgements

Conflict of interest and funding

There is no conflict of interest in the present study for any of the authors.

References

1. Henkel RE, Bova D, Dillehay GL, Karesh SM, Halama JR, Wagner RH, editors. Nuclear medicine, second ed. Philadelphia, PA: Elsevier; 2006.
2. Lin E, Alavi A. editors. PET and PET/CT: a clinical guide. New York: Thieme; 2005.
3. Cherry SR, Sorensen JA, Phelps ME. Physics in nuclear medicine, Philadelphia, PA: WB Saunders Company; 2003.
4. Valk PE, Bailey DE, Townsend DW, Maisey MN. Positron emission tomography: basic science and clinical practice. New York: Springer; 2003.
5. Wernick MN, Aarsvold JN. Emission tomography. Philadelphia, PA: Academic Press; 2004.
6. Kak AC, Slaney M. Principles of computerized tomographic imaging. New York: IEEE Press; 1988.
7. Hudson HM, Larkin RS. Accelerated image reconstruction using ordered subsets of projection data. IEEE Trans Med Imaging 1994; 13: 601–9.
8. Kinahan PE, Hasegawa BH, Beyer T. X-ray-based attenuation correction for positron emission tomography/computed tomography scanners. Semin Nucl Med 2003; 33: 166–79.
9. Bergstrom M, Ericksson L, Bohm C, Blomqvist G, Litton J. Correction for scattered radiation in a ring detector positron camera by integral transformation of projections. J Comput Assist Tomogr 1983; 7: 42–50.
10. Ollinger JM. Detector efficiency and Compton scatter in fully 3D PET. IEEE Trans Nucl Sci 1995; 42: 1168–73.
11. Hoffman EJ, Huang SC, Phelps ME, Kuhl DE. Quantitation in positron emission tomography: 4. Effect of accidental coincidences. J Comput Assist Tomogr 1981; 5: 391–400.
12. Daube-Witherspoon ME, Karp JS, Casey ME, DiFilippo FP, Hines H, Muehllehner G, et al. PET performance measurements using the NEMA NU 2-2001 standard. J Nucl Med 2002; 43: 1398–409.
13. Phelps ME, Hoffman EJ, Huang S-C, Ter-Pogossian MM. Effect of positron range on spatial resolution. J Nucl Med 1975; 6: 649–52.
14. DeBenedetti S, Cowan CE, Konneker WR, Primakoff H. On the angular distribution of two-photon annihilation radiation. Phys Rev 1950; 77: 205–LP: -212.
15. Hoffman EJ, Huang SC, Plummer D, Phelps ME. Quantitation in positron emission tomography: 6. effect of nonuniform resolution. J Comput Assist Tomogr 1982; 6: 987–99.
16. Beyer T, Townsend D, Brun T, Kinahan P, Charron M, Roddy R, et al. A combined PET/CT scanner for clinical oncology. J Nucl Med 2000; 41: 1369–79.
17. Ding Y, Gatley SJ. Positron radiopharmaceuticals and their chemistry. In: Henkel RE, Bova D, Dillehay GL, Karesh SM, Halama JR, Wagner RH, eds. Nuclear medicine, second ed. Philadelphia, PA: Elsevier; 2006: 439–56.
18. Vallabhajosula S. ^{18}F-labeled positron emission tomographic radiopharmaceuticals in oncology: an overview of radiochemistry and mechanisms of tumor localization. Semin Nucl Med 2007; 37: 400–19.
19. Richmond DR, Tauxe WN, Bassingthwaighte JB. Albumin macroaggregates and measurements of regional blood flow: validity and application of particle sizing by Coulter counter. J Lab Clin Med 1970; 75: 336–46.
20a. Yipintsoi T, Dobbs WA Jr, Scanlon PD, Knopp TJ, Bassingthwaighte JB. Regional distribution of diffusible tracers and carbonized microspheres in the left ventricle of isolated dog hearts. Circ Res 1973; 33: 573–87.
20b. Bassingthwaighte JB, Malone MA, Moffett TC, King RB, Chan IS, Link JM, et al. Molecular and particulate depositions for regional myocardial flows in sheep. Circ Res 1990; 66: 1328–44.
21. Berman DS, Hachamovitch R, Kiat H, Cohen I, Cabico A, Wang FW, et al. Incremental value of prognostic testing in patients with known or suspected ischemic heart disease: a basis for optimal utilization of exercise technetium-99m sestamibi myocardial perfusion single photon emission computed tomography. J Am Coll Cardiol 1992; 26: 639–47.
22. Hachamovitch R, Berman DS, Kiat H, Cohen I, Lewin H, Amanullah A, et al. Incremental prognostic value of adenosine stress myocardial perfusion single-photon emission computed tomography and impact on subsequent management in patients with or suspected of having myocardial ischemia. Am J Cardiol 1997; 80: 426–33.
23. Hachamovitch R, Hayes S, Friedman JD, Cohen I, Shaw LJ, Germano G, et al. Determinants of risk and its temporal variation in patients with normal stress myocardial perfusion scans: what is the warranty period of a normal scan? J Am Coll Cardiol 2003; 41: 1329–40.
24. Kong BA, Shaw L, Miller DD, Chaitman BR. Comparison of accuracy for detecting coronary artery disease and side-effect profile of dipyridamole thallium-201 myocardial perfusion imaging in women versus men. Am J Cardiol 1992; 70: 168–73.
25. Nishimura S, Mahmarian J, Boyce T, Verani M. Quantitative thallium-201 single-photon emission computed tomography during maximal pharmacologic coronary vasodilation with adenosine for assessing coronary artery disease. J Am Coll Cardiol 1991; 18: 736–45.
26. Bateman T, Maddahi J, Gray R, Murphy F, Garcia E, Conklin C, et al. Diffuse slow washout of myocardial thallium-201: a new scintigraphic indicator of extensive coronary artery disease. J Am Coll Cardiol 1983; 4: 55–64.
27. Jadvar H, Strauss HW, Segall GM. SPECT and PET in the evaluation of coronary artery disease. RadioGraphics 1999; 19: 915–26.
28. Schuijf J, Poldermans D, Shaw L, Jukema J, Lamb H, de Roos A, et al. Diagnostic and prognostic value of non-invasive imaging in known or suspected coronary artery disease. Eur J Nucl Med 2006; 33: 93–104.
29. Bateman TM, Heller GV, McGhie AI, Friedman JD, Case JA, Bryngelson JR, et al. Diagnostic accuracy of rest/stress ECG-gated Rb-82 myocardial perfusion PET: comparison with ECG-gated Tc-99m sestamibi SPECT. J Nucl Cardio 2006; 13: 24–33.
30. Freedman N, Schechter D, Klein M, Marciano R, Rozenman Y, Chisin R. SPECT attenuation artifacts in normal and overweight persons: insights from a retrospective comparison of Rb-82 positron emission tomography and Tl-201 SPECT myocardial perfusion imaging. Clin Nucl Med 2000; 25: 1019–23.
31. Yoshinaga K, Chow BJW, Williams K, Chen L, deKemp RA, Garrard L, et al. What is the prognostic value of myocardial perfusion imaging using rubidium-82 positron emission tomography? J Am Coll Cardiol 2006; 48: 1029–39.

32. Machac J. Cardiac positron emission tomography imaging. Sem Nucl Med 2005; 35: 17–36.

33. Bergmann SR, Fox KA, Rand AL, McElvany KD, Welch MJ, Markham J, et al. Quantification of regional myocardial blood flow in vivo with H_2O-15. Circulation 1984; 70: 724–33.

34. Hutchins GD, Schwaiger M, Rosenspire KC, Krivokapich J, Schelbert H, Kuhl DE. Noninvasive quantification of regional blood flow in the human heart using N-13 ammonia and dynamic positron emission tomographic imaging. J Am Coll Cardiol 1990; 15: 1032–42.

35. Muzik O, Beanlands R, Hutchins G, Mangner T, Nguyen N, Schwaiger M. Validation of nitrogen-13-ammonia tracer kinetic model for quantification of myocardial blood flow using PET. J Nucl Med 1993; 34: 83–91.

36. van den Hoff J, Burchert W, Borner AR, Fricke H, Kuhnel G, Meyer GJ, et al. [1-^{11}C]Acetate as a quantitative perfusion tracer in myocardial PET. J Nucl Med 2001; 42: 1174–82.

37. Herrero P, Markham J, Shelton M, Bergmann S. Implementation and evaluation of a two-compartment model for quantification of myocardial perfusion with rubidium-82 and positron emission tomography. Circ Res 1992; 70: 496–507.

38. Lacy JL, Haynes NG, Nayak N, Mathias CJ, Wallhaus TR, Stewart R, et al. A PET myocardial perfusion imaging with generator produced radiopharmaceuticals. ^{62}Cu-PTSM and ^{62}Cu-ETS. Clin Positron Imaging 1999; 2: 317.

39. Madar I, Ravert HT, Du Y, Hilton J, Volokh L, Dannals RF, et al. Characterization of uptake of the new PET imaging compound ^{18}F-fluorobenzyl triphenyl phosphonium in dog myocardium. J Nucl Med 2006; 47: 1359–66.

40. deKemp RA, Yoshinaga K, Beanlands RSB. Will 3-dimensional PET-CT enable the routine quantification of myocardial blood flow? J Nucl Card 2007; 14: 380–97.

41. Tancredi RG, Yipintsoi T, Bassingthwaighte JB. Capillary and cell wall permeability to potassium in isolated dog hearts. Am J Physiol 1975; 229: 537–44.

42. Bassingthwaighte JB. A concurrent flow model for extraction during transcapillary passage. Circ Res 1974; 35: 483–503.

43. Bassingthwaighte JB, Goresky CA. Modeling in the analysis of solute and water exchange in the microvasculature. In: Renkin EM, Michel CC, eds. Handbook of physiology. Sect. 2, The cardiovascular system. Vol IV, The microcirculation. Bethesda, MD: The American Physiological Society; 1984. p. 549–626.

44. Krivokapich J, Smith G, Huang S, Hoffman E, Ratib O, Phelps M. ^{13}N ammonia myocardial imaging at rest and with exercise in normal volunteers. Quantification of absolute myocardial perfusion with dynamic positron emission tomography. Circulation 1989; 80: 1328–37.

45. Crone C. The permeability of capillaries in various organs as determined by the use of the 'indicator diffusion' method. Acta Physiol Scand 1963; 58: 292–305.

46. Renkin EM. Exchangeability of tissue potassium in skeletal muscle. Am J Physiol 1959; 197: 1211–5.

47. Yoshida K, Mullani N, Gould KL. Coronary flow and flow reserve by PET simplified for clinical applications using rubidium-82 or nitrogen-13-ammonia. J Nucl Med 1996; 37: 1701–12.

48. Huang SC, Williams BA, Krivokapich J, Araujo L, Phelps ME, Schelbert HR. Rabbit myocardial 82Rb kinetics and a compartmental model for blood flow estimation. Am J Physiol 1989; 256: H1156–64.

49. Khorsand A, Graf S, Pirich C, Muzik O, Kletter K, Dudczak R, et al. Assessment of myocardial perfusion by dynamic N-13 ammonia PET imaging: comparison of 2 tracer kinetic models. J Nucl Cardiol 2005; 12: 410–7.

50. Deussen A, Bassingthwaighte JB. Modeling [^{15}O]oxygen tracer data for estimating oxygen consumption. Am J Physiol Heart Circ Physiol 1996; 270: H1115–30.

51. Caldwell JH, Williams DL, Harp GD, Stratton JR, Ritchie JL. Quantitation of size of relative myocardial perfusion defect by single-photon emission computed tomography. Circulation 1984; 70: 1048–56.

52. Yipintsoi T, Bassingthwaighte JB. Circulatory transport of iodoantipyrine and water in the isolated dog heart. Circ Res 1970; 27: 461–77.

53. Cormode DP, Skajaa T, Fayad ZA, Mulder WJ. Nanotechnology in medical imaging: probe design and applications. Arterioscler Thromb Vasc Biol 2009; 29: 992–1000.

54. Devaraj NK, Keliher EJ, Thurber GM, Nahrendorf M, Weissleder R. ^{18}F labeled nanoparticles for in vivo PET-CT imaging. Bioconjug Chem 2009; 20: 397–401.

55. Nakamura K, Wang Y, Liu X, Kubo A, Hnatowich DJ. Cell culture and xenograft-bearing animal studies of radiolabeled antisense DNA carrier nanoparticles with streptavidin as a linker. J Nucl Med 2007; 48: 1845–52.

56. Pressly ED, Rossin R, Hagooly A, Fukukawa K, Messmore BW, Welch MJ, et al. Structural effects on the biodistribution and positron emission tomography (PET) imaging of well-defined ^{64}Cu-labeled nanoparticles comprised of amphiphilic block graft copolymers. Biomacromolecules 2007; 8: 3126–34.

57. Fukukawa K, Rossin R, Hagooly A, Pressly ED, Hunt JN, Messmore BW, et al. Synthesis and characterization of core-shell star copolymers for in vivo PET imaging applications. Biomacromolecules 2008; 9: 1329–39.

58. Welch MJ, Hawker CJ, Wooley KL. The advantages of nanoparticles for PET. J Nucl Med 2009; 50: 1743–6.

59. Nahrendorf M, Zhang H, Hembrador S, Panizzi P, Sosnovik DE, Aikawa E, et al. Nanoparticle PET-CT imaging of macrophages in inflammatory atherosclerosis. Circulation 2008; 117: 379–87.

60. Weissleder R, Kelly K, Sun EY, Shtatland T, Josephson L. Cell-specific targeting of nanoparticles by multivalent attachment of small molecules. Nat Biotechnol 2005; 23: 1418–23.

61. Choi HS, Liu W, Misra P, Tanaka E, Zimmer JP, Itty Ipe B, et al. Renal clearance of quantum dots. Nat Biotechnol 2007; 25: 1165–70.

*James B. Bassingthwaighte
Departments of Bioengineering and Radiology
University of Washington
Seattle, WA 98295-5061, USA
Email: jbb2@uw.edu